Title

Substrate utilization and cross-feeding synergistically determine microbiome resistance to pathogen invasion

Authors

Xinrun Yang[1,#], Tianjie Yang[1,#,*], Ziru Zhang[1], Yaozhong Zhang[1], Xinlan Mei[1], Yang Gao[1], Ningqi Wang[1], Gaofei Jiang[1], Yangchun Xu[1], Qirong Shen[1], Zhong Wei[1,*], Alexandre Jousset[1]

Xinrun Yang: 0000-0002-6482-8734 xinrunyang@stu.njau.edu.cn

Tianjie Yang: 0000-0003-0927-2670 tjyang@njau.edu.cn

Ziru Zhang: 0009-0005-8683-777X zhangzr@stu.njau.edu.cn

Yaozhong Zhang: 0000-0002-8024-6523 yaozhongzyz@stu.njau.edu.cn

Xinlan Mei: 0000-0003-4408-5184 meixinlan@njau.edu.cn

Yang Gao: 0009-0005-8962-8631 gaoyang@njau.edu.cn

Ningqi Wang: 0000-0002-7788-4364 wangnq@njau.edu.cn

Gaofei Jiang: 0000-0002-5331-739X gjiang@njau.edu.cn

Yangchun Xu: 0000-0003-2740-5561 ycxu@njau.edu.cn

Qirong Shen: 0000-0002-5662-9620 shenqirong@njau.edu.cn

Zhong Wei: 0000-0002-7967-4897 weizhong@njau.edu.cn

Alexandre Jousset: 0000-0002-6805-2486 jousset@njau.edu.cn

# These authors contributed equally to this work.

Affiliation

[1] Jiangsu Provincial Key Lab for Solid Organic Waste Utilization, Key Lab of Organic-based Fertilizers of China, Jiangsu Collaborative Innovation Center for Solid Organic Wastes, Educational Ministry Engineering Center of Resource-saving fertilizers, Nanjing Agricultural University, Nanjing 210095, China

[*]**Correspondence**

Email: tjyang@njau.edu.cn (Tianjie Yang)

Email: weizhong@njau.edu.cn (Zhong Wei)

Abstract

Understanding how microbiomes resist pathogen invasion remains a key challenge in natural ecosystems. Here, we combined genome-scale metabolic models with synthetic community experiments to unravel the mechanisms driving pathogen suppression. We developed curated genome-scale models for each strain, incorporating 48 common resource utilization profiles to fully capture their metabolic capacities. Trophic interactions inferred from models accurately predicted pathogen invasion outcomes, achieving 93% accuracy across 620 invasion tests involving diverse microbial communities and nutrient environments. Importantly, considering both substrate and metabolite features provided a more holistic understanding of pathogen suppression. In particular, cross-feeding metabolites within the native community emerged as crucial yet often overlooked predictors of community resistance, disproportionally favoring native species over invaders. This study lays the foundation for designing disease-resistant microbiomes, with broad implications for mitigating pathogen exposure in diverse environments.

Introduction

The host-associated microbiome functions as a critical defense line against invading pathogens[1,2]. While it is well-established that high microbiome diversity limits pathogen invasion[3–6], the underlying mechanisms remain unclear. Increasing evidence suggests that resource utilization patterns play a pivotal role in determining pathogen invasion[7,8]. Specifically, substrate competition—both between the resident microbial community and the pathogen, as well as within the resident community itself—has emerged as a key factor in driving community resistance to pathogen invasion[7,9]. Despite the important role of substrate competition, the importance of microbial metabolites in pathogen suppression has largely been overlooked. Cross-feeding metabolites, defined as compounds secreted by one strain and utilized by another[10], are key determinants of microbial interactions that may influence pathogen suppression[11,12]. Thus, understanding the dual role of substrate competition and metabolite exchange is critical to fully appreciating how microbiomes protect their host from pathogen invasion.

Predicting trophic interactions in multispecies communities has long been limited by the experimental challenges involved. *In vitro* experiments designed to examine substrate and metabolite features are already labor-intensive under controlled conditions and become increasingly impractical in complex natural settings[13], where species composition and environmental conditions are highly variable[14,15]. Genome-scale metabolic models offer a promising solution to these challenges[16]. Using genome data, standardized pipelines can now rapidly generate metabolic models, enabling *in silico* predictions of resource utilization, metabolite secretion, and growth rates[17,18]. These models have the potential to predict metabolic interactions within community contexts, linking community composition and functional traits with susceptibility to pathogen invasion across diverse nutritional environments[19,20].

In this study, we used defined plant-associated microbial communities to assess the predictive power of genome-scale models in explaining patterns of pathogen invasion. The plant root environment contains a host-specific set of plant-derived labile carbon compounds, which fuels the development of a host-specific microbiome[21]. These nutrients are accessible to both commensals and pathogens, and imbalances in resource utilization can promote disease[2,22]. While previous studies have primarily focused on substrate availability as a driver of pathogen invasion[7], we hypothesize that considering both substrate and metabolite features offers a more comprehensive mechanism for pathogen suppression, with microbial cross-feeding playing an equally important but less understood role in contributing to community resistance to pathogen invasion (Fig. 1A). To test this hypothesis, we constructed resident communities of plant-associated bacteria and challenged them with invasion by the plant pathogen *Ralstonia solanacearum* (Table S1). These isolates were selected due to nutrient competition being their main mechanism for pathogen suppression, eliminating confounding effects from secondary metabolites[23]. We conducted *in vitro* resource utilization experiments to fully characterize the metabolic capacity of each strain, subsequently refining models to address apparent gaps in purely genomics-based models. These models were then used to predict pathogen invasion, as well as the associated substrate and metabolite features (Fig. 1B). Finally, we validated these predictions experimentally, offering key insights into how microbial substrate and metabolite features contribute to pathogen suppression.

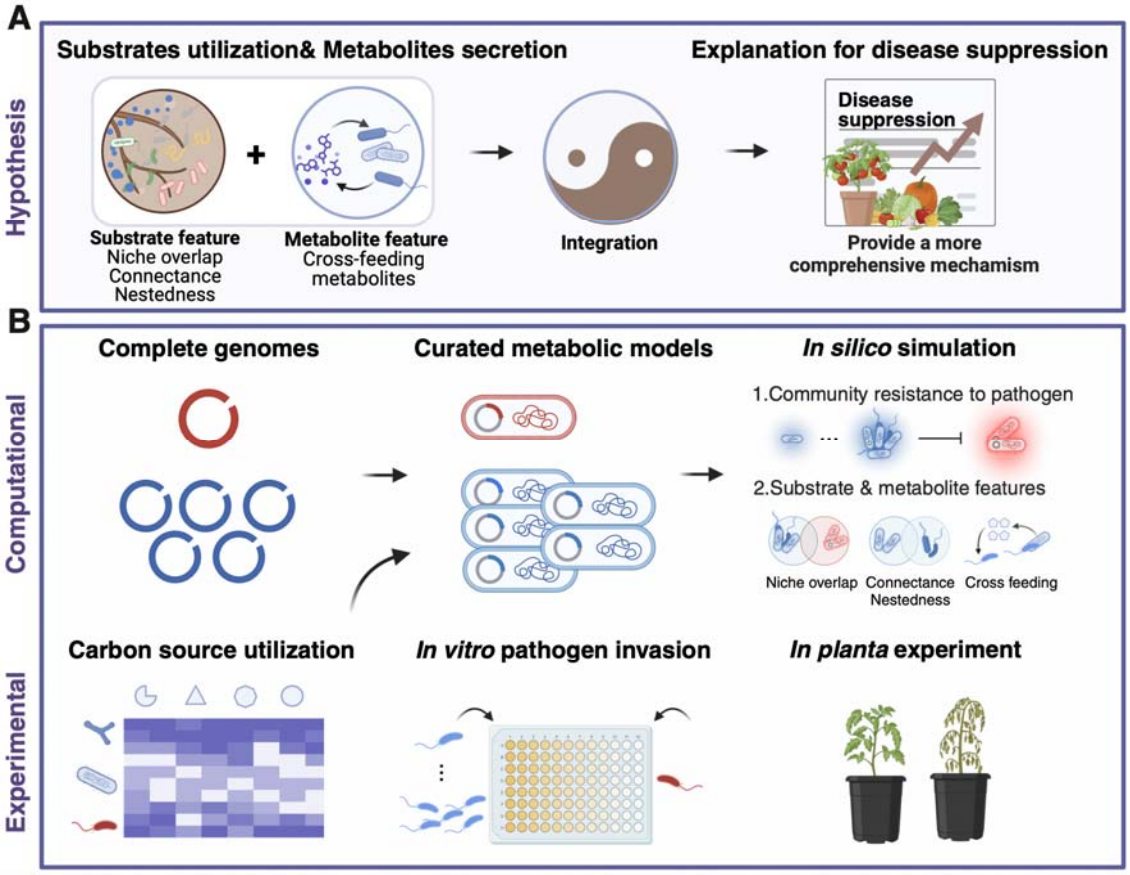

Fig. 1 Hypothesis and the workflow. (**A**) Hypothesis scenarios. Plant roots release abundant carbon substrates that attract both native species and pathogens. The resident community can suppress invading pathogens by outcompeting them for nutrient substrate. However, the role of microbial metabolites in pathogen suppression is not well understood. We hypothesize that considering both substrate and metabolite features offers a more comprehensive understanding of disease suppression. In particular, microbial cross-feeding, although less explored, is likely to play a significant role in enhancing community resistance to pathogen invasion. (**B**) Experimentally and computationally guided workflow. Genome-scale metabolic models were constructed for both the pathogen and the resident community, based on genomic data and carbon source utilization profiles. Flux balance analysis was employed to simulate pathogen invasion and metabolic features across different community configurations and carbon source environments. These *in silico* predictions were then validated through *in vitro* and *in planta* experiments, offering key insights into the mechanisms underlying microbial community-mediated pathogen suppression.

Results

In silico simulation of pathogen invasion and metabolic features

We initially conducted *in vitro* carbon source utilization assays using 48 environmentally relevant substrates to characterize the metabolic capacity of each strain (Fig. 2A). Draft models based solely on genomic data showed limited accuracy in predicting substrate utilization profiles, due to incomplete genome annotations and missing key metabolic pathways, which constrained their predictive power[20]. To address this, we curated genome-scale models by incorporating experimental carbon source utilization data to fill these gaps for each growth-supporting carbon source. This refinement significantly improved the accuracy of substrate utilization predictions, with a mean improvement of 52% (Student's paired *t* test: t = -5.1, df = 5.0, P = 0.004, Fig. 2B). Next, we employed these models to simulate community resistance to pathogen invasion across a wide range of community and nutritional environments. This involved 620 pathogen invasion tests spanning 31 SynCom combinations (covering all possible species richness and community compositions, Table S3) and 20 randomly selected carbon source combinations (Table S4). Notably, our results demonstrated strong predictive capabilities of SynComs in pathogen suppression, achieving 93% accuracy (Fig. 2C). We further used genome-scale models to predict substrate and metabolite features. To represent substrate features, we included three variables—nestedness, connectance, and niche overlap—based on our previous work[7]. Niche overlap reflects substrate competition between native species and invader, nestedness and connectance describes substrate competition within native species. Our findings revealed a strong correlation between predicted and observed substrate features (R^2 > 0.85, Fig. 2D), enabling us to incorporate the observed substrate features into subsequent analyses. For metabolite features, we predicted three variables—total produced metabolites, extracellular metabolites, and cross-feeding metabolites—to capture the metabolite exchanges within microbial community (Fig. 2E). The number of these metabolites effectively limit pathogen invasion both *in vitro* and *in planta* (Fig. 3A-B), suggesting the importance of microbial metabolite in pathogen suppression. During microbial cross-feeding, strain QL-A2 displayed the highest frequency of absorbing metabolites (*ANOVA*, $F_{4,95}$ = 67.1, P < 0.001), while strain QL-140 showed the highest frequency (*ANOVA*, $F_{4,95}$ = 284.9, P < 0.001) of producing metabolites (Fig. S1).

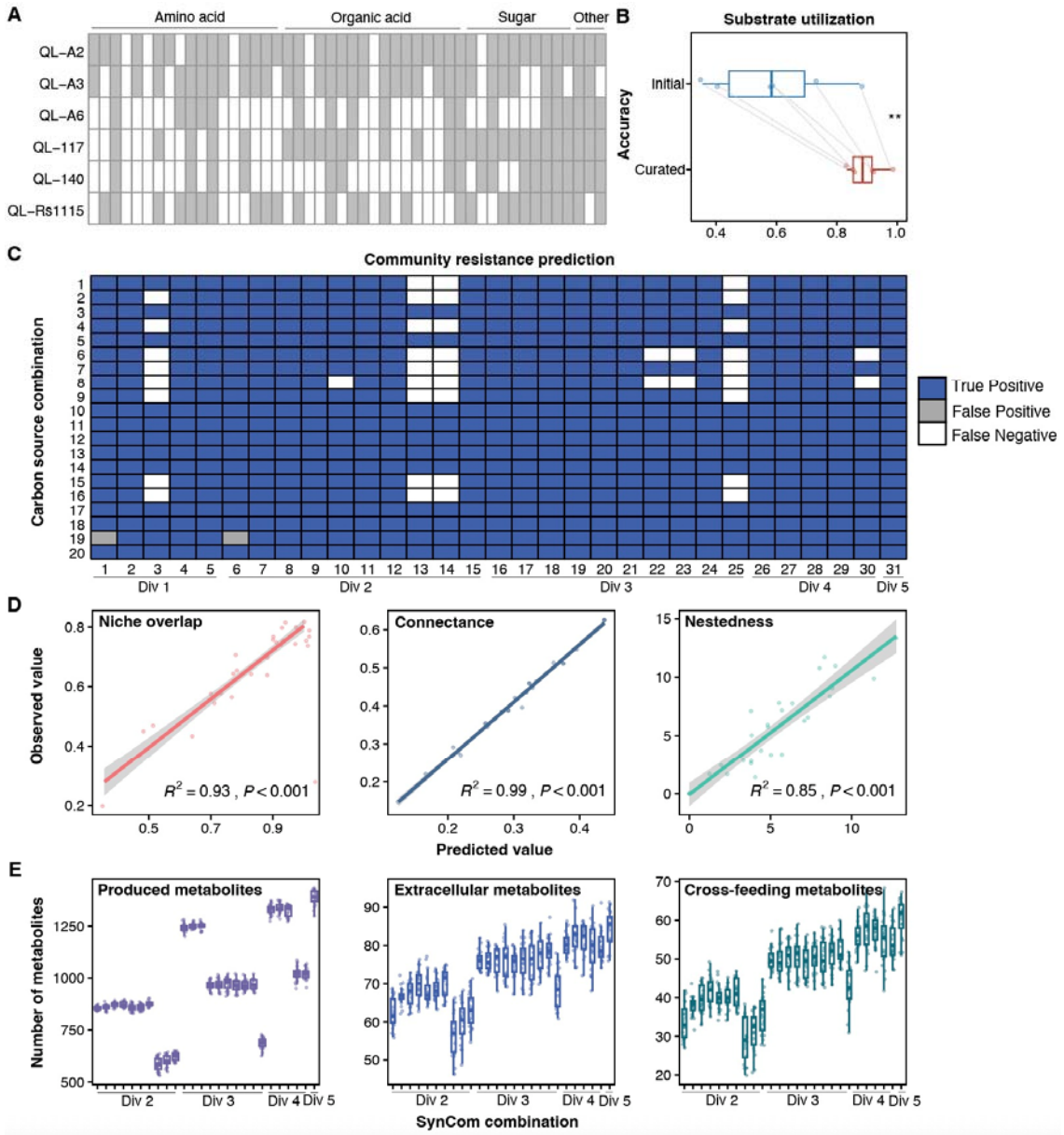

Fig. 2 Modeling predictions for pathogen invasion and metabolic features. (**A**) Experimental carbon source utilization profiles of 48 common resources in the rhizosphere for each strain. The fill color of the boxes indicates whether growth occurred (grey) or did not occur (white) for each carbon resource. (**B**) Comparison of prediction accuracy for carbon source utilization between solely genomic-based models and curated models. Curated models were constructed through gap-filling based on the experimental carbon source utilization profiles of each strain. *P* values were calculated using pairwise Student's *t*-tests (**P* < 0.05, ***P* < 0.01). (**C**) Prediction accuracy matrix of putative interactions between 31 SynCom communities and the pathogen under 20 randomly selected carbon source combinations. Interactions are inferred by comparing pathogen growth in coculture versus monoculture. (**D**) Linear regression between predicted substrate features and observed substrate features. The R^2 and *P* values denote the goodness of fit and significance level of linear regression, respectively. (**E**) Prediction of the number of total produced metabolites, extracellular metabolites, and cross-feeding metabolites under the same community and nutritional conditions as the *in vitro* pathogen invasion experiments. Only SynComs with a richness greater than 1 were included, as cross-feeding requires at least two microbial members for effective interaction. The dots in the boxplot represent the number of each metabolite under 20 carbon resource combinations.

136
137 **Considering both substrate and metabolite features improves explanation of pathogen suppression**
138 In addition to *in vitro* pathogen invasion experiments, we extended our research to a greenhouse setting
139 using tomato plants grown in sterile planting substrate, applying the same 31 SynCom treatments used in
140 the *in vitro* assays. By combing data from both the *in vitro* and *in planta* experiments, we aimed to
141 determine whether incorporating substrate and metabolite features could more effectively explain
142 community resistance to pathogen invasion. Given the crucial role of cross-feeding metabolites in
143 explaining community resistance to pathogen invasion, as observed across all metabolite features in both
144 *in vitro* and *in planta* experiments (*in vitro*: R^2=0.30, *in planta*: R^2= 0.67, Fig. 3A-B), we incorporated cross-
145 feeding metabolites with substrate features—nestedness, connectance, and niche overlap and employed
146 generalized linear models (GLMs) to explore the explanation for pathogen suppression (Table 1). Our
147 results revealed that considering both substrate and metabolite features offered a more comprehensive
148 explanation for pathogen suppression than using community diversity, substrate features, or cross-
149 feeding individually (Table 1 and Fig. 3C). This integration resulted in an average increase in explanatory
150 power of 54.96%, 28.99%, and 31.98%, respectively (Fig. 3C). Remarkably, cross-feeding metabolites
151 consistently emerged as significant predictors across all *in vitro* and *in planta* experiments when analyzed
152 through stepwise regression (Table 1), highlighting the crucial role of cross-feeding in enhancing
153 community resistance to pathogen invasion.

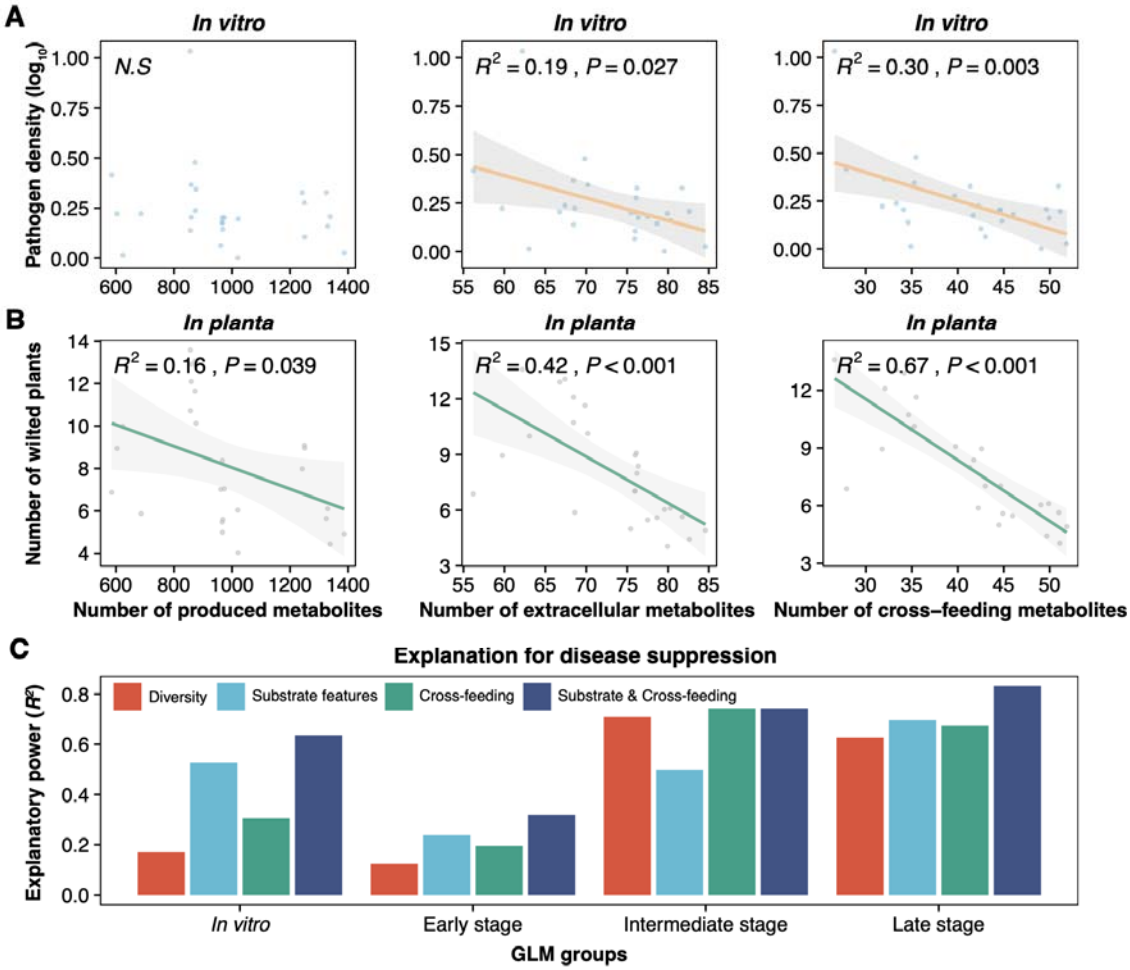

154
155 **Fig. 3 Impact of considering both substrate and metabolite features on explaining pathogen**
156 **suppression.** (**A**) Linear regression between the number of total produced, extracellular, and cross-
157 feeding metabolites and pathogen density. Only SynCom with a richness greater than 1 were included, as
158 effective cross-feeding requires the presence of at least two microbial members for interaction. The dots
159 represent the average number of metabolites in 20 different carbon resource combinations. (**B**) Linear
160 regression between the number of total produced, extracellular, and cross-feeding metabolites and

disease severity. Disease severity is measured by the number of wilted plants. (**C**) Comparison of the explanatory power for pathogen suppression between models considering both substrate and metabolite features versus those considering only community diversity, substrate features, and cross-feeding, based on generalized linear models (GLMs) results. Explanatory power is quantified by R^2 values obtained from GLMs analyses.

Table 1 Comparison of the explanation of pathogen suppression between models that incorporate both substrate and metabolite features and those that consider diversity alone, based on generalized linear models (GLMs) results.

	d.f.	*In vitro*		*In planta*					
		Pathogen density		Early stage		Intermediate stage		Late stage	
		t value	*P*-value	t value	*P*-value	t value	*P*-value	t value	*P*-value
SynCom diversity	1	-2.22	0.03	-1.84	0.08	-7.66	<0.0001	-6.35	<0.0001
Model summary		R^2: 0.17↓	AIC: -9.62	R^2: 0.12↓	AIC: 105.44	R^2: 0.71↓	AIC: -10.44	R^2: 0.63 ↓	AIC: 108.41
Nestedness (NE)	1	Not retained		-1.44	0.16	Not retained		-1.74	0.09
Connectance (CO)	1	Not retained		Not retained		Not retained		**-3.33**	**0.003**
Niche overlap (NOI)	1	**-2.71**	**0.013**	Not retained		Not retained		Not retained	
Cross-feeding (CF)	**1**	**-2.12**	**0.04**	**-3.27**	**0.003**	**-8.29**	**<0.0001**	**-5.83**	**<0.0001**
NE*CF	1	Not retained		1.88	0.07	Not retained		Not retained	
CO*CF	1	Not retained		Not retained		Not retained		Not retained	
NOI*CF	1	1.90	0.07	1.49	0.15	Not retained		Not retained	
Model summary		**R^2: 0.64↑**	AIC: -27.04	**R^2: 0.32↑**	AIC: 100.95	**R^2: 0.74↑**	AIC: -13.41	**R^2: 0.83↑**	AIC: 91.60

Disease dynamics were assessed by fitting the disease progression curves using logistic regression, which captures three key stages: lag time before disease onset (early stage), exponential rate of disease spread (intermediate stage), and asymptotic disease saturation (late stage). The SynCom diversity denoted the richness of the resident community (continuous variable). The arrows in the model summary indicate the relative explanatory power of diversity-based GLMs versus metabolic feature-based GLMs in pathogen suppression, with upward arrows representing higher explanatory power and downward arrows indicating lower explanatory power. The table presents the most parsimonious models, selected based on the AIC information criterion through backward and forward model selection.

Mechanism of cross-feeding metabolites in pathogen suppression

Given the important role of predicted cross-feeding metabolites in conferring community resistance to pathogen invasion observed in both *in vitro* and *in planta* experiments, we aimed to validate their function and elucidate the underlying mechanism. We first selected the SynCom with the highest richness (richness = 5) and conducted *in silico* simulations by randomly selecting ten selected cross-feeding and ten non-crossfeeding metabolites from 48 carbon sources pool, repeating 99 times. Our simulations demonstrated that cross-feeding metabolites significantly suppressed pathogen density compared to non-crossfeeding metabolites (Student's *t* test: $t = -18.9$, $df = 119.8$, $P < 0.0001$, Fig. 4A). This finding was further confirmed through *in vitro* experiments under same community and metabolite conditions (Student's *t* test: $t = -2.7$, $df = 193.5$, $P = 0.007$, Fig. 4A). We hypothesize that pathogens have limited ability to utilize cross-feeding metabolites, while the native microbial community effectively leverages these metabolites to promote its growth (Fig. 4B). To test this hypothesis, we conducted an additional *in vitro* experiment comparing SynCom biomass and pathogen density under cross-feeding and non-crossfeeding metabolite conditions. The results showed significantly lower pathogen densities (Student's *t* test: $t = -28.9$, $df = 184.9$, $P < 0.0001$, Fig. 4C) and higher SynCom growth (Student's *t* test: $t = 2.66$, $df = 184.1$, $P = 0.009$, Fig. 4C) in the presence of cross-feeding metabolites. Furthermore, we observed a negative correlation between SynCom biomass and pathogen density in the presence of cross-feeding metabolites (Fig. S2). These findings confirm that pathogens are less effective at utilizing cross-feeding metabolites, while these metabolites enhance SynCom growth.

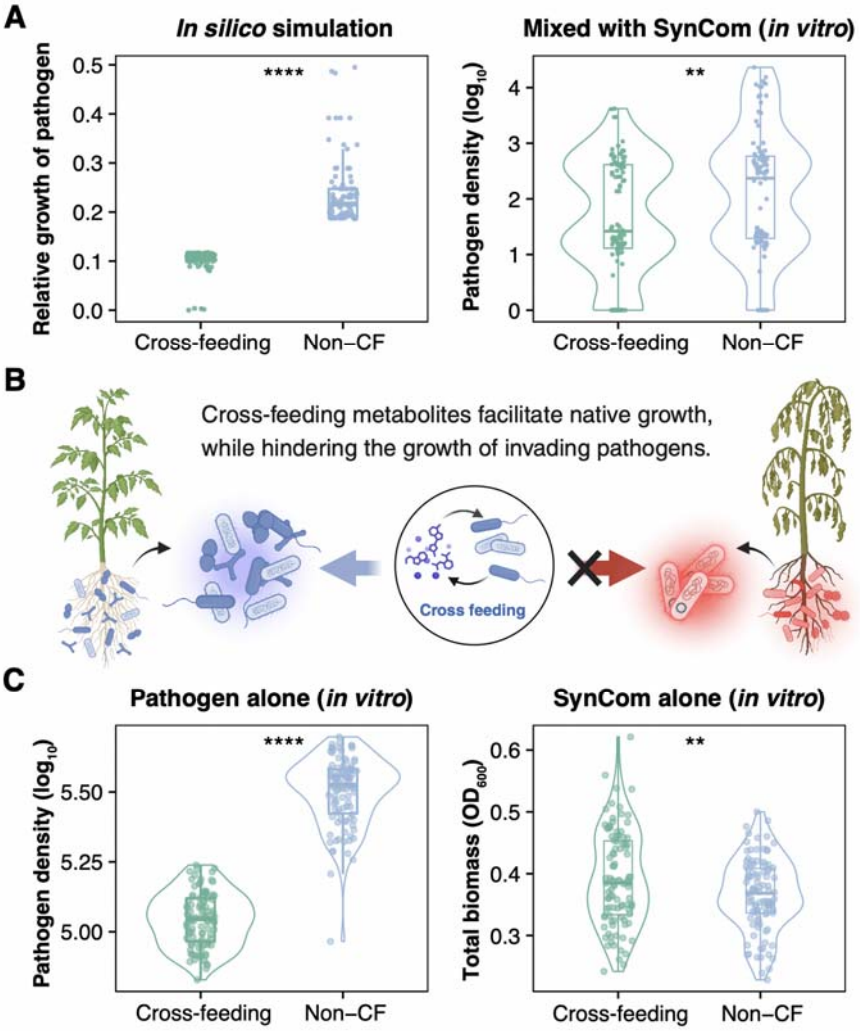

Fig. 4 Experimental validation of the role cross-feeding metabolites in pathogen suppression. (**A**) Comparison of the pathogen growth and density with the addition of cross-feeding metabolites versus non-crossfeeding metabolites, as observed in both *in silico* simulation and *in vitro* validation. Non-CF denotes non-crossfeeding metabolites. The relative pathogen growth is defined as the ratio of pathogen growth to the resident community growth. (**B**) Schematic illustrating the hypothesis that pathogens are less efficient at utilizing cross-feeding metabolites, while these metabolites enhance the growth of native species. (**C**) Comparison of *in vitro* pathogen density and SynCom growth with the addition of cross-feeding metabolites versus non-crossfeeding metabolites. *P* values were calculated using Student's *t*-tests (**P* < 0.05; ***P* < 0.01; ****P* < 0.001; *****P* < 0.0001).

Discussion

In this study, we investigated the utility of genome-scale metabolic models in predicting pathogen invasion across diverse microbial communities and nutritional environments, shedding light on the mechanisms underlying microbiome resistance against pathogen invasion. Our findings demonstrate the strong performance of genome-scale models in predicting community resistance to pathogen invasion, achieving 93% accuracy across 620 invasion tests. This highlights the promising role of genome-scale models as a valuable tool for the targeted design of disease-resistant microbiomes, offering potential strategies to mitigate pathogen-related risks in microbial ecosystems. Moreover, our results indicated that considering both substrate and metabolite features offered a more robust explanation for microbiome resistance to pathogen invasion than community diversity, substrate feature, or cross-feeding alone. Notably, cross-feeding metabolites emerged as an a critical but often overlooked factor in conferring resistance against pathogen invasion. Subsequent *in vitro* experiments revealed the mechanism behind these metabolites, showing that pathogens struggle to utilize those cross-feeding metabolites, while these metabolites enhance the vigor and competitiveness of the resident community. Overall, our study not only emphasizes the crucial role of genome-scale models in predicting community resistance to pathogen invasion but also highlights the importance of considering substrate and metabolite features to better explaining pathogen suppression.

Differences in substrate utilization profiles between models based solely on genomic data and those informed by experimental data have been widely reported. This discrepancy is often attributed to inherent gaps and inaccuracies in genome annotations[24], failing to fully capture the true metabolic capacities of strains[25,26]. When key metabolic pathways are absent or improperly annotated, strains struggle to utilize certain growth-supporting resources effectively, leading to incorrect predictions about their biomass production under different environmental conditions[27]. Therefore, *in vitro* carbon source utilization profiles were used for gap-filling to refine the models, which allowed us to create more robust and reliable models capable of simulating and predicting the microbial interactions in various nutritional environments[26]. In addition to gap-filling based on the carbon source screen, the strains in our study exhibit metabolic competition without direct antagonism may provide a solid foundation for exploring their interactions and the underlying metabolic mechanisms based on genome-scale models[28]. Moreover, future research could integrate more experimental and multi-omics data, such as growth curves, transcriptomics, and metabolomics, which allow for a more detailed understanding of gene expression and metabolite fluxes, thereby improving the quantitative predictive power[29]. Future research could include a larger and more diverse community to explore the predictive accuracy in pathogen invasions and the design of beneficial communities targeted to suppress specific pathogens more effectively.

Cross-feeding plays a pivotal role in pathogen suppression by promoting cooperation and maintaining functional diversity within microbial communities[30,31]. It facilitates the exchange and recycling of essential metabolites among microbes and ensures a relatively balanced ecosystem[32]. This collaborative resource sharing through cross-feeding is particularly important for creating a robust defense against invading pathogens, as it enhances the community's collective metabolic capabilities[33]. In healthy microbiomes, cross-feeding networks contribute to metabolic redundancy and cooperation, where different microbes contribute to the overall fitness and stability of the community[34]. However, when cross-feeding networks break down, as seen in dysbiotic states, the balance of resource sharing is disrupted[35]. Dysbiosis often results in a loss of functional diversity, where certain microbes are outcompeted or eliminated, leaving gaps in resource utilization. Pathogens can exploit these gaps, utilizing unclaimed nutrients and proliferating in the absence of competition[11].

From an evolutionary perspective, cross-feeding reflects processes such as Black Queen evolution[36], where some species lose the ability to produce certain metabolites and instead rely on other members of the community to provide them. In this scenario, cross-feeding is not just a cooperative behavior but an evolutionary necessity, where metabolic functions are distributed among different species[37]. As microbial species evolve to specialize and share metabolic functions, they form a tightly interconnected community where each member plays a critical role in maintaining overall function[38]. The co-adaptive nature of cross-feeding helps explain why disruptions in these networks, such as those caused by environmental changes or antibiotic use, can lead to pathogen susceptibility. In the absence of effective cross-feeding, pathogens can more easily invade and disrupt the functional balance of microbiomes, but strong cross-feeding networks acts as a metabolic buffer, enhancing the community resistance to pathogens[34].

In summary, our study highlights the utility of genome-scale models in predicting community resistance to pathogen invasion across diverse nutritional environments and in elucidating the underlying metabolic mechanisms determining this resistance. This paves the way for the targeted design of disease-resistant microbiomes. By considering both substrate and metabolite features, we offer a more comprehensive understanding of the factors contributing to microbiome resistance within diverse microbiomes. This work not only advances our understanding of microbial interactions but also offers practical applications for improving ecosystem health.

Methods

Bacterial strains

The phytopathogen used in this study was *Ralstonia solanacearum* QL-Rs1115, which was tagged with the pYC12-mCherry plasmid[39]. Additionally, we utilized five nonvirulent *Ralstonia* strains (*Ralstonia mannitolilytica* QL-A2, *Ralstonia mannitolilytica* QL-A3, *Ralstonia pickettii* QL-A6, *Ralstonia* sp. QL-117, *Ralstonia pickettii* QL-140) as commensal species[7]. Notably, no antagonistic interactions were detected either among the commensal species or between the commensal species and the phytopathogen[23]. All strains were routinely maintained at -80 ℃ with glycerol (final concentration of 20%). Further details on the bacterial strains and plasmid were listed in Table S1.

Carbon source utilization experiment

Each strain was cultured in Nutrient Broth (NB) medium (composed of glucose 10.0 g L^{-1}, peptone 5.0 g L^{-1}, yeast extract 0.5g L^{-1}, beef extract 3.0g L^{-1}, pH 7.0) at 30 ℃ until reaching the exponential growth phase. Subsequently, cells were harvested by centrifugation at 6000 rpm for 6 minutes, washed three times with 0.85% NaCl buffer, and resuspended in OS minimal medium[40] to an optical density at 600 nm (OD_{600}) of 0.1. The bacterial suspension was then transferred to 150 µL OS minimal medium supplemented with a specific resource in individual wells of 96-well plates, with six replicates per resource condition. We used 48 commonly detected resources from tomato rhizosphere to represent environmental substrates (Table S2). OS minimal medium without any resource was used as the negative control. After 48 h growth at 30 ℃ with agitation, optical density of the single strain was measured using a SpectraMax M5 Plate reader (Molecular Devices, Sunnyvale, CA, USA). Wells with an $OD_{600} > 0.05$ were considered as positive growth on the respective resource.

In vitro pathogen invasion experiment

Prior to the experiment, a single colony of each strain was selected and grown overnight on Nutrient Agar (NA, NB medium with agar 18 g L^{-1}). The bacterial cultures were subsequently washed three times with 0.85% NaCl buffer and adjusted to an OD_{600} of ~0.5, approximately 10^7 CFU ml^{-1}. We systematically assembled 31 microbial communities covering all possible species diversity and community compositions (Table S3), following substitutive designs[41]. Then, each SynCom was established with an initial total bacterial density of 10^7 CFU mL^{-1} to ensure consistency across all combinations, and the ratios of strains in SynComs with richness above 2 were equal. Next, SynComs were inoculated into 20 different resource combinations to simulate various nutritional environments (Table S4), resulting in a total of 620 pathogen invasion experiments (31 communities x 20 nutritional environments, Table S5). Specifically, each SynCom consisted of OS minimal medium supplemented with a random mixture of 20 resources selected from a total pool of 48 resources. The SynComs were then exposed to invasion by the mCherry-tagged *R. solanacearum* QL-Rs1115 strain (at a concentration of 10^5 cells per ml) in 96-well plates (200 µl per well) at 30 ℃ with agitation, while SynComs grown alone in the absence of the pathogen served as negative controls. SynCom growth was assessed after 48 hours based on OD_{600}, while pathogen growth was evaluated based on mCherry fluorescence signal (excitation: 587 nm, emission: 610 nm). Next, we adjusted the red fluorescent protein signals (RFP) by subtracting the RFP measured in the negative control (absence of the pathogen) from the RFP measured in the presence of the pathogen. We then calculated pathogen density using the formula $\log_{10}(RFP/OD_{600})$. A successful invasion was defined as a scenario where the pathogen density was greater than 0 and the RFP of the treatment with the pathogen exceeded the average RFP value of the negative control without the pathogen. Only communities that experienced successful invasion were considered for further analysis[7]. An interaction was defined as suppression if pathogen density in coculture was less than 90% of that in monoculture. Conversely, it was defined as facilitation if these values were more than 110% of those in monoculture[20].

Greenhouse experiment

A 42-day greenhouse experiment was conducted to investigate the inhibitory effect of 31 SynComs against the pathogen. Consistent with our *in vitro* experiments, we utilized the same 31 SymComs with two replicates each, with positive controls containing only the pathogen (three replicates), and negative controls without any bacteria (three replicates). Tomato seeds (Lycopersicon esculentum, cultivar 'Jiangshu') were surface-sterilized and germinated on a water agar plate for 3 days before being transferred to seedling plates containing cobalt-60-sterilized seedling substrate sourced from the Huainong Institute of Soil and Fertilizer, Huaian, China. At the three-leaf stage (11 days after seeding), tomato plants were then transplanted into seedling trays containing the same seedling substrate and

323 inoculated with SynCom via drenching, resulting in an ending concentration of 10^8 CFU/g soil[42]. The
324 invasion experiment started after 1 week by inoculating the pathogen, resulting in a final concentration
325 of 10^6 CFU/g soil. Throughout the experiment, the greenhouse maintained a temperature range of 25-
326 35 °C and was regularly watered with sterile water to ensure optimal tomato growth. To mitigate bias,
327 the seedling pots were randomly rearranged every 2 days. Daily monitoring of the number of wilted
328 seedlings per plate from day 17 after transplantation. Given the inability to directly quantify available
329 rhizosphere carbon resources, we assumed that all 48 resources utilized in our *in vitro* experiments were
330 available in the rhizosphere. Disease dynamics was evaluated using a logistic growth curve that tracked
331 the percentage of wilted plants as a function of time throughout the experiment's duration. This curve
332 fitting yielded three variables: the lag phase (days after pathogen inoculation) before disease onset, the
333 intrinsic rate of increase of wilted plants (day^{-1}), and the asymptotic disease prevalence (% of wilted
334 plants), which are respectively referred to as the early, intermediate, and late stages of infection.
335 **DNA extraction and genome sequencing**
336 The genomic DNA extraction of six strains was performed using a Bacteria DNA Kit (OMEGA) following the
337 manufacturer's instructions, with subsequent quality control of the purified DNA samples. Genomic DNA
338 was quantified using a TBS-380 fluorometer (Turner BioSystems Inc., Sunnyvale, CA). High-quality DNA
339 samples ($OD_{260/280}$=1.8~2.0, >6 μg) were used to construct fragment libraries. The genomes of the strains
340 were sequenced employing a combination of PacBio RS and Illumina sequencing platforms. For Pacific
341 sequencing, 20 kb insert whole-genome shotgun libraries were prepared and sequenced on a Pacific
342 Biosciences RS instrument using standard protocols. An aliquot of 8 μg DNA was spun in a Covaris g-TUBE
343 (Covaris, MA) at 6,000 RPM for 60 seconds using an Eppendorf 5424 centrifuge (Eppendorf, NY). DNA
344 fragments were then purified, end-repaired, and ligated with SMRTbell sequencing adapters following
345 the manufacturer's recommendations (Pacific Biosciences, CA). Resulting sequencing libraries were
346 purified three times using 0.45x volumes of Agencourt AMPure XP beads (Beckman Coulter Genomics,
347 MA) following the manufacturer's recommendations. For Illumina sequencing, at least 3 μg of genomic
348 DNA was used for library construction. Paired-end libraries with insert sizes of approximately 400 bp
349 were prepared following Illumina's standard genomic DNA library preparation protocol. Purified genomic
350 DNA was sheared into smaller fragments with a desired size by Covaris, and blunt ends were generated
351 using T4 DNA polymerase. After adding an 'A' base to the 3' end of the blunt phosphorylated DNA
352 fragments, adapters were ligated to the ends of the DNA fragments. The desired fragments were purified
353 through gel electrophoresis, then selectively enriched and amplified by PCR. The index tag could be
354 introduced into the adapter at the PCR stage as appropriate, and a library quality test was performed.
355 The qualified Illumina paired-end library was then used for Illumina NovaSeq 6000 sequencing (150 bp * 2,
356 Shanghai BIOZERON Co., Ltd). The raw paired-end reads were trimmed and quality controlled by
357 Trimmomatic[43] with the parameters (SLIDINGWINDOW: 4:15 MINLEN:75). Clean data obtained from the
358 quality control processes were used for further analysis. Illumina sequencing data was used to evaluate
359 the complexity of the genome and correct the PacBio long reads. ABySS[44] was used for genome assembly
360 with multiple-Kmer parameters to obtain the optimal assembly results, and Canu[45] was used to assemble
361 the PacBio-corrected long reads. GapCloser[46] was subsequently applied to fill up the remaining local inner
362 gaps and correct the single base polymorphisms for the final assembly results. The quality assessment of
363 these genomes was conducted using CheckM[47], revealing an average completeness of 99.88% (Table S1).
364 **Construction of genome-scale metabolic models**
365 The gapseq[48] tool was employed to construct genome-scale metabolic models and perform gap-filling.
366 This tool utilizes various data sources and a novel gap-filling procedure, enhancing the versatility of
367 metabolic models for predicting physiological responses under various chemical growth conditions[48].
368 Initially, metabolic models were generated based on the assembled genomes of each strain.
369 Subsequently, we compared the predicted carbon source utilization of each draft model with
370 experimental data from carbon source utilization assays, and those carbon sources that the strain could
371 utilize but were not accurately predicted by the model were identified. We then used gapseq to perform
372 gap-filling on each graft model to generate a new set of biosynthesis and transport reactions, allowing
373 the model to produce biomass from each growth-supporting carbon source identified in our experiments.
374

375 **Computing predicted pathogen growth in monoculture and coculture based on genome-scale models**

376 We utilized COBRApy[49] with the CPLEX solver v12.10 (IBM) in Python 3.7 to compute the pathogen
377 growth in both monoculture and coculture conditions. Similar to our *in vitro* experiments, the simulated
378 medium consisted of OS minimal medium and 20 random resources. The models were provided with
379 nonlimiting amounts (v_{max} = 1000 mmol gDW^{-1} $hour^{-1}$) of the simulated OS minimal medium components
380 (Table S6), including essential carbon dioxide, metal ions, water, and nitrogen, sulfur, and phosphorus
381 sources. Additionally, limiting amounts (v_{max} = 0.1 mmol gDW^{-1} $hour^{-1}$) of the resources were supplied in
382 the medium. For the SynCom models, individual strain models were integrated into a shared extracellular
383 compartment[50,51], with all metabolites, reactions, and genes, except those in the extracellular
384 compartment, specifically labeled. Biomass was set as the objective function for model growth
385 simulations. To simulate an equal abundance of resources between monoculture and coculture
386 conditions, the sum of biomass reactions was set as the objective to be optimized, and exchange reaction
387 values were adjusted to match those of the models in monoculture. The predicted pathogen growth is
388 based on the biomass fluxes of the pathogen. For each pair or community, we first simulated the biomass
389 fluxes of the pathogen when grown alone. Subsequently, we recorded the biomass fluxes of the
390 pathogen when cocultured with the SynCom. Effective pathogen suppression by the SynCom was
391 determined if the biomass flux of pathogen in coculture was lower than that observed in 90% of
392 pathogen grown alone. Conversely, if the biomass of pathogen in coculture exceeded 110% of the
393 biomass of pathogen grown alone, it was considered that the SynCom promoted pathogen growth[20].

394 **Computing metabolite features within the SynCom based on genome-scale models**

395 The predicted numbers of produced metabolites, extracellular metabolites, and cross-feeding
396 metabolites within the SynComs were calculated based on COBRApy[49] with the CPLEX solver v12.10 (IBM)
397 in Python 3.7. Metabolites produced by one strain and absorbed by another within the communities
398 were identified as cross-feeding metabolites, which include both mutualistic and exploitative
399 interactions[10]. Considering the cross-feeding requires the presence of two or more strains, we only
400 included the SynComs with a richness at least 2 in our predictions of produced metabolites and
401 extracellular metabolites.

402 **Additional *in vitro* validation experiment**

403 To further investigate the role of cross-feeding metabolites in suppressing pathogen invasion, we
404 conducted additional validation experiments based on *in silico* simulation and *in vitro* experiment. We
405 began by selecting the resident community with the highest richness (richness = 5) to maximize their
406 cross-feeding potential. From our pool of carbon sources, we randomly selected 10 cross-feeding
407 metabolites and 10 non-crossfeeding metabolites to predict the pathogen growth when the resident
408 community was cocultured with the pathogen *in silico*, repeating 99 times. Following the *in silico*
409 conditions, we conducted an *in vitro* experiment using the same community and nutritional
410 environments. We conducted three different treatments: (1) pathogen grown alone, (2) pathogen
411 cocultured with the resident community, and (3) resident community cultured alone. We then measured
412 the RFP and OD_{600} to evaluate pathogen density and SynCom biomass.

413 **Data analysis**

414 Analysis of variance (ANOVA) were performed using the aov() function of the stats package. Linear
415 regressions were used to explore the relationship between metabolic features and pathogen density.
416 General linear models (GLMs) were employed to assess the explanatory power of metabolic features and
417 community diversity in pathogen suppression. Due to potential correlations among metabolic features,
418 we used stepwise model selection (step() function of the stats package) to identify the optimal GLMs.
419 Student's *t*-tests were used to test statistical significance between pairs of samples, where *P* value below
420 0.05 were considered statistically significant. If not stated otherwise, all data processing, statistical
421 analyses, and graphical representation were performed in R 4.1.3 (www.r-project.org).
422

Data availability

The genome sequences and metabolic models are available on Zenodo (10.5281/zenodo.14007949).

Code availability

The scripts used for analysis are available on Zenodo (10.5281/zenodo.14008038).

Acknowledgements

We thank Jiaheng Hou from Peking University for insightful discussions and suggestions. This research was funded by the National Natural Science Foundation of China (42325704, 42477125, and 42090060), the Fundamental Research Funds for the Central Universities (KYT2024001), the Natural Science Foundation of Jiangsu Province (BK20230102), and the Jiangsu Carbon Peak & Carbon Neutrality Science and Technology Innovation Special Fund (BE2022423).

Author contributions

Conceptualization: X.Y., T.Y. and Z.W.; Resources: T.Y., A.J., and Z.W.; Methodology: X.Y. T.Y., and A.J.; Data curation: X.Y., Z.Z., Y.Z., N.W., and G.J.; Formal analysis: X.Y., Z.Y., and N.W.; Funding acquisition: T.Y., G.J, Y.C., and Q.S. and Z.W.; Investigation: X.Y., T.Y., Z.Z., Y.Z., N.W., and G.J.; Project Administration: T.Y., Z.W., Y.C., and Q.S.; Supervision: T.Y., Z.W., Y.C., and Q.S.; Software: X.Y., T.Y.; Visualization: X.Y., T.Y., Y.Z., and A.J.; Writing—original draft: X.Y., T.Y. and A.J.; Writing—review & editing: T.Y., A.J., and Z.W.

Declaration of interests

The authors declare no competing interests.

442 **References**

443 1. De Vos, W. M., Tilg, H., Van Hul, M. & Cani, P. D. Gut microbiome and health: mechanistic
444 insights. *Gut* **71**, 1020–1032 (2022).

445 2. Berendsen, R. L., Pieterse, C. M. J. & Bakker, P. A. H. M. The rhizosphere microbiome and plant
446 health. *Trends in Plant Science* **17**, 478–486 (2012).

447 3. Fassarella, M. *et al.* Gut microbiome stability and resilience: elucidating the response to
448 perturbations in order to modulate gut health. *Gut* **70**, 595–605 (2021).

449 4. Hu, J. *et al.* Probiotic Diversity Enhances Rhizosphere Microbiome Function and Plant Disease
450 Suppression. *mBio* **7**, e01790-16 (2016).

451 5. Yang, T. *et al.* Resource availability modulates biodiversity-invasion relationships by altering
452 competitive interactions. *Environmental Microbiology* **19**, 2984–2991 (2017).

453 6. Yang, X. *et al.* High microbiome diversity constricts the prevalence of human and animal
454 pathogens in the plant rhizosphere worldwide. *One Earth* **7**, 1301–1312 (2024).

455 7. Wei, Z. *et al.* Trophic network architecture of root-associated bacterial communities determines
456 pathogen invasion and plant health. *Nature Communications* **6**, 8413 (2015).

457 8. Spragge, F. *et al.* Microbiome diversity protects against pathogens by nutrient blocking. *Science*
458 **382**, eadj3502 (2023).

459 9. Michalska-Smith, M. *et al.* Network structure of resource use and niche overlap within the
460 endophytic microbiome. *The ISME Journal* **16**, 435–446 (2022).

461 10. Culp, E. J. & Goodman, A. L. Cross-feeding in the gut microbiome: Ecology and mechanisms. *Cell*
462 *Host & Microbe* **31**, 485–499 (2023).

463 11. Semenec, L. *et al.* Cross-protection and cross-feeding between Klebsiella pneumoniae and
464 Acinetobacter baumannii promotes their co-existence. *Nat Commun* **14**, 702 (2023).

465 12. Oña, L. *et al.* Obligate cross-feeding expands the metabolic niche of bacteria. *Nat Ecol Evol* **5**,
466 1224–1232 (2021).

467 13. Pacheco, A. R. & Vorholt, J. A. Resolving metabolic interaction mechanisms in plant microbiomes.
468 *Current Opinion in Microbiology* **74**, 102317 (2023).

469 14. Mateos, D. M. & Bhatnagar, J. M. Restoring ecological complexity in a changing environment.
470 *Current Biology* **34**, R365–R371 (2024).

471 15. Romdhane, S. *et al.* Land-use intensification differentially affects bacterial, fungal and protist
472 communities and decreases microbiome network complexity. *Environmental Microbiome* **17**, 1 (2022).

473 16. Cottret, L. *et al.* MetExplore: a web server to link metabolomic experiments and genome-scale
474 metabolic networks. *Nucleic Acids Research* **38**, W132–W137 (2010).

475 17. Price, N. D., Reed, J. L. & Palsson, B. Ø. Genome-scale models of microbial cells: evaluating the
476 consequences of constraints. *Nat Rev Microbiol* **2**, 886–897 (2004).

477 18. Fang, X., Lloyd, C. J. & Palsson, B. O. Reconstructing organisms in silico: genome-scale models and
478 their emerging applications. *Nat Rev Microbiol* **18**, 731–743 (2020).

479 19. Magnúsdóttir, S. *et al.* Generation of genome-scale metabolic reconstructions for 773 members
480 of the human gut microbiota. *Nat Biotechnol* **35**, 81–89 (2017).

481 20. Schäfer, M. *et al.* Metabolic interaction models recapitulate leaf microbiota ecology. *Science*
482 (2023).

483 21. Ling, N., Wang, T. & Kuzyakov, Y. Rhizosphere bacteriome structure and functions. *Nat Commun*
484 **13**, 836 (2022).

485 22. Berg, G., Eberl, L. & Hartmann, A. The rhizosphere as a reservoir for opportunistic human
486 pathogenic bacteria. *Environmental Microbiology* **7**, 1673–1685 (2005).

487 23. Wei, Z. *et al.* Efficacy of Bacillus-fortified organic fertiliser in controlling bacterial wilt of tomato
488 in the field. *Applied Soil Ecology* **48**, 152–159 (2011).

489 24. Thiele, I. & Palsson, B. Ø. A protocol for generating a high-quality genome-scale metabolic
490 reconstruction. *Nat Protoc* **5**, 93–121 (2010).

491 25. Mendoza, S. N., Olivier, B. G., Molenaar, D. & Teusink, B. A systematic assessment of current
492 genome-scale metabolic reconstruction tools. *Genome Biol* **20**, 158 (2019).

493 26. Bernstein, D. B., Sulheim, S., Almaas, E. & Segrè, D. Addressing uncertainty in genome-scale
494 metabolic model reconstruction and analysis. *Genome Biol* **22**, 64 (2021).

495 27. Ankrah, N. Y. D. *et al.* Enhancing Microbiome Research through Genome-Scale Metabolic
496 Modeling. *mSystems* **6**, e00599-21 (2021).

497 28. Du, H., Li, M. & Liu, Y. Towards applications of genome-scale metabolic model-based approaches
498 in designing synthetic microbial communities. *Quant. Biol.* **11**, 15 (2023).

499 29. Xu, X., Lv, X., Bi, X., Chen, J. & Liu, L. Genetic circuits for metabolic flux optimization. *Trends in*
500 *Microbiology* S0966842X24000040 (2024) doi:10.1016/j.tim.2024.01.004.

501 30. Smith, N. W., Shorten, P. R., Altermann, E., Roy, N. C. & McNabb, W. C. The Classification and
502 Evolution of Bacterial Cross-Feeding. *Front. Ecol. Evol.* **7**, (2019).

503 31. Henriques, S. F. *et al.* Metabolic cross-feeding in imbalanced diets allows gut microbes to
504 improve reproduction and alter host behaviour. *Nat Commun* **11**, 4236 (2020).

505 32. Mataigne, V., Vannier, N., Vandenkoornhuyse, P. & Hacquard, S. Microbial Systems Ecology to
506 Understand Cross-Feeding in Microbiomes. *Front. Microbiol.* **12**, (2021).

507 33. Paasch, B. C. & He, S. Y. Toward understanding microbiota homeostasis in the plant kingdom.
508 *PLoS Pathog* **17**, e1009472 (2021).

509 34. Marcelino, V. R. *et al.* Disease-specific loss of microbial cross-feeding interactions in the human
510 gut. *Nat Commun* **14**, (2023).

511 35. Arnault, G., Mony, C. & Vandenkoornhuyse, P. Plant microbiota dysbiosis and the Anna Karenina
512 Principle. *Trends in Plant Science* S1360138522002187 (2022) doi:10.1016/j.tplants.2022.08.012.

513 36. Morris, J. J. Black Queen evolution: the role of leakiness in structuring microbial communities.
514 *Trends in Genetics* **31**, 475–482 (2015).

515 37. Estrela, S., Trisos, C. H. & Brown, S. P. From Metabolism to Ecology: Cross-Feeding Interactions
516 Shape the Balance between Polymicrobial Conflict and Mutualism. *The American Naturalist* **180**, 566–576
517 (2012).

518 38. Kost, C., Patil, K. R., Friedman, J., Garcia, S. L. & Ralser, M. Metabolic exchanges are ubiquitous in
519 natural microbial communities. *Nat Microbiol* **8**, 2244–2252 (2023).

520 39. Gu, S. *et al.* Competition for iron drives phytopathogen control by natural rhizosphere
521 microbiomes. *Nat Microbiol* **5**, 1002–1010 (2020).

522 40. Schnider-Keel, U. *et al.* Autoinduction of 2,4-Diacetylphloroglucinol Biosynthesis in the Biocontrol
523 Agent *Pseudomonas fluorescens* CHA0 and Repression by the Bacterial Metabolites Salicylate and
524 Pyoluteorin. *J Bacteriol* **182**, 1215–1225 (2000).

525 41. Johnson, P. T. J., Preston, D. L., Hoverman, J. T. & Richgels, K. L. D. Biodiversity decreases disease
526 through predictable changes in host community competence. *Nature* **494**, 230–233 (2013).

527 42. Wei, Z. *et al.* The congeneric strain Ralstonia pickettii QL-A6 of Ralstonia solanacearum as an
528 effective biocontrol agent for bacterial wilt of tomato. *Biological Control* **65**, 278–285 (2013).

529 43. Bolger, A. M., Lohse, M. & Usadel, B. Trimmomatic: a flexible trimmer for Illumina sequence data.
530 *Bioinformatics* **30**, 2114–2120 (2014).

531 44. Jackman, S. D. *et al.* ABySS 2.0: resource-efficient assembly of large genomes using a Bloom filter.
532 *Genome Res.* **27**, 768–777 (2017).

533 45. Koren, S. *et al.* Canu: scalable and accurate long-read assembly via adaptive *k* -mer weighting and
534 repeat separation. *Genome Res.* **27**, 722–736 (2017).

535 46. Xu, M. *et al.* TGS-GapCloser: A fast and accurate gap closer for large genomes with low coverage
536 of error-prone long reads. *GigaScience* **9**, giaa094 (2020).

537 47. Parks, D. H., Imelfort, M., Skennerton, C. T., Hugenholtz, P. & Tyson, G. W. CheckM: assessing the
538 quality of microbial genomes recovered from isolates, single cells, and metagenomes. *Genome Res.* **25**,
539 1043–1055 (2015).

540 48. Zimmermann, J., Kaleta, C. & Waschina, S. gapseq: informed prediction of bacterial metabolic
541 pathways and reconstruction of accurate metabolic models. *Genome Biol* **22**, 81 (2021).

542 49. Ebrahim, A., Lerman, J. A., Palsson, B. O. & Hyduke, D. R. COBRApy: COnstraints-Based
543 Reconstruction and Analysis for Python. *BMC Syst Biol* **7**, 74 (2013).

544 50. Heinken, A. & Thiele, I. Anoxic Conditions Promote Species-Specific Mutualism between Gut
545 Microbes *In Silico*. *Appl Environ Microbiol* **81**, 4049–4061 (2015).

546 51. Klitgord, N. & Segre, D. Environments that Induce Synthetic Microbial Ecosystems. *PLoS*
547 *Computational Biology* **6**, (2010).

548